Article

Electrostatics, Charge Transfer, and the Nature of the Halide−Water Hydrogen Bond

Published as part of The Journal of Physical Chemistry virtual special issue "Daniel Neumark Festschrift".

John M. Herbert* and Kevin Carter-Fenk

Read Online

ACCESS | Metrics & More | Article Recommendations | Supporting Information

ABSTRACT: Binary halide−water complexes $X^-(H_2O)$ are examined by means of symmetry-adapted perturbation theory, using charge-constrained promolecular reference densities to extract a meaningful charge-transfer component from the induction energy. As is known, the $X^-(H_2O)$ potential energy surface (for X = F, Cl, Br, or I) is characterized by symmetric left and right hydrogen bonds separated by a C_{2v}-symmetric saddle point, with a tunneling barrier height that is <2 kcal/mol except in the case of $F^-(H_2O)$. Our analysis demonstrates that the charge-transfer energy is correspondingly small (<2 kcal/mol except for X = F), considerably smaller than the electrostatic interaction energy. Nevertheless, charge transfer plays a crucial role determining the conformational preferences of $X^-(H_2O)$ and provides a driving force for the formation of quasi-linear X··· H−O hydrogen bonds. Charge-transfer energies correlate well with measured O−H vibrational redshifts for the halide−water complexes and also for $OH^-(H_2O)$ and $NO_2^-(H_2O)$, providing some indication of a general mechanism.
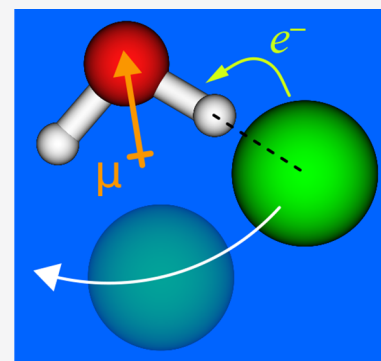
1. INTRODUCTION

Halide−water clusters are archetypal systems for understanding anion−water hydrogen bonds and have been studied extensively with gas-phase vibrational spectroscopy,[1−3] from which it has been established that the binding motif involves a single ion−water hydrogen bond per water molecule. This conclusion is in agreement with *ab initio* calculations,[4−11] some of which predate the experiments.[4−8] For the binary complexes $X^-(H_2O)$, the coordination motif is not the C_{2v}-symmetric structure that one might naively anticipate based on the orientation of the H_2O dipole moment vector. Nevertheless, popular general chemistry textbooks continue to illustrate the hydration of small, monatomic anions such as Cl^- in this dipole-centric way.[12,13] This work reports the application of energy decomposition analysis to investigate the competition between "dipolar" (C_{2v}-symmetric) coordination versus asymmetric HOH···X^- hydrogen bonding, with the latter emerging as the minimum-energy structure for X = F, Cl, Br, and I.

It has long been appreciated that vibrational frequency shifts engendered by hydrogen bonding can be understood on the basis of charge transfer (CT),[14−22] providing a theoretical explanation for the observed correlation between hydrogen bond strength and O−H vibrational frequency shift (the "Badger−Bauer rule").[21−25] The specific case of anion−water hydrogen bonding has been considered in detail,[26−28] but the basic idea is the same: $X^- \rightarrow \sigma^*_{OH}$ CT populates antibonding orbitals and thus manifests as a redshift in the hydrogen-bonded O−H stretching vibration, with respect to that of a free O−H moiety. What is notable about the anion−water case is

the magnitude of the shift: e.g., a bit more than 2000 cm^{-1} in the case of $F^-(H_2O)$ and almost 3000 cm^{-1} in the case of $OH^-(H_2O)$.[1−3]

A one-dimensional view of $X^-(H_2O)$ is presented in Figure 1, consisting of a symmetric double-well potential along the angle θ_{XOH}. The minima represent quasi-linear hydrogen bonds (HB_L and HB_R in Figure 1), with the C_{2v} geometry as a saddle
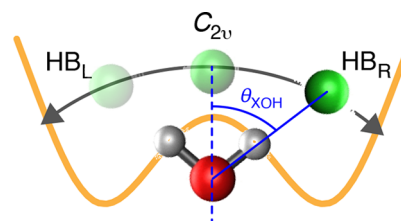

Figure 1. Schematic depiction of $X^-(H_2O)$ along the angular coordinate θ_{XOH} that connects the left and right hydrogen-bonded structures, HB_L and HB_R. In the background is a double-well potential illustrating that the two quasi-linear hydrogen bonds are local minima but that the C_{2v} "dipolar" geometry is a saddle point.

Table 1. Optimized Geometries of $X^-(H_2O)$ Complexes[a]

| | hydrogen-bonded | | | | | C_{2v} saddle point | | |
| | distance (Å) | | | angle (deg) | | distance (Å) | | angle (deg) |
X	$r(XH_1)$	$r(OH_1)$[b]	$r(OH_2)$[b]	$\theta(XH_1O)$	$\theta(HOH)$[c]	$r(XH)$	$r(OH)$[b]	$\theta(HOH)$[c]
F	1.370	1.065	0.960	177.7	101.9	2.002	0.975	89.7
Cl	2.115	0.991	0.961	168.9	100.6	2.574	0.969	96.3
Br	2.289	0.986	0.961	167.5	100.6	2.708	0.969	95.9
I	2.559	0.981	0.961	164.5	100.6	2.950	0.968	97.2

[a]MP2/aug-cc-pVTZ(-PP) level. [b]Value for an isolated H_2O monomer is $r(OH) = 0.961$ Å. [c]Value for an isolated H_2O monomer is $\theta(HOH) = 104.1°$.

point in between. There have been numerous calculations of the anharmonic vibrational frequencies of $X^-(H_2O)$ complexes,[4,10,29−37] including calculations of the $HB_L \leftrightarrow HB_R$ tunneling splitting.[29−37] This splitting has been measured experimentally in $I^-(H_2O)$,[2,37] but is much smaller (and not observed) in $F^-(H_2O)$ due to the much stronger hydrogen bond and concomitantly larger barrier height. The very strong hydrogen bond in $F^-(H_2O)$ manifests as extreme anharmonicity along the hydrogen-bonded O−H stretching coordinate,[4] and the corresponding vibrational frequency is shifted to lower energy even than the free H_2O bend at 1590 cm^{-1}.[2,3] The anharmonicity can be explained in terms of a low-energy crossing between diabatic states representing $F^- + H_2O$ and $FH + OH^-$,[2,27] which explains why the redshifts in various anion−water complexes correlate with the proton affinity of the anion.[2,3,38]

Vibrational spectroscopy is not the focus of the present work, however. Rather, our aim is to understand why the double-well potential exists in the first place, or in other words, to clarify what driving forces stabilize the hydrogen bonds as compared to the dipolar C_{2v} geometry, the latter of which might have been anticipated based on electrostatic arguments that remain widely taught in general chemistry.[12,13] The primary tool in this analysis will be symmetry-adapted perturbation theory (SAPT),[39−42] which is a form of energy decomposition analysis that is specifically designed for intermolecular interactions. Isolated monomer wave functions (for X^- and H_2O, in the present work) serve as zeroth-order states and perturbation theory is used to incorporate their interaction, with individual terms in the perturbation expansion that are readily classified as electrostatics, Pauli (or exchange) repulsion, induction, and dispersion.

We also anticipate a major role for CT, as discussed above. The quantitative description of this effect, however, has been historically problematic in both SAPT and in most other energy decomposition analyses, where it is difficult to separate from polarization.[43] Although the sum of polarization and CT can be made reasonably well-defined, attempts to separate the two are often exquisitely sensitive to the underlying atomic orbital (AO) basis set, with very different answers obtained in double-ζ basis sets as compared to higher-quality basis sets that might approach the complete-basis limit.[43]

Two seemingly workable solutions have emerged that allow a well-defined CT energy (E_{CT}) to be extracted from the SAPT induction energy.[43−47] One strategy is based on regularization of the nuclear Coulomb potentials on one monomer or the other, thus eliminating the driving force for intermolecular CT and using this to isolate E_{CT} from the SAPT induction energy, E_{ind}.[47] That approach is not pursued here. Instead, we consider an alternative definition of E_{CT} that is based on the machinery

of charge-constrained density functional theory (cDFT).[48] In this approach, cDFT is used to define a CT-free reference state, in which the monomers may polarize one another while their charge densities are constrained to integrate to integer numbers of electrons. Subsequent lifting of that constraint defines E_{CT}, with $E_{ind} - E_{CT}$ defining the true (CT-free) polarization energy.[43−46]

The present work reports an improved implementation of the SAPT + cDFT approach as compared to the one reported previously by our group.[43] We then apply this method to understand the $X^-(H_2O)$ potential curves such as the one depicted schematically in Figure 1.

2. THEORY AND METHODS

All calculations were performed using Q-Chem, v. 5.3.[49] Several modifications to Q-Chem are reported as part of this work, most notably fragment-based Hirshfeld weights for cDFT.

2.A. Geometries and Benchmarks. Geometries for $X^-(H_2O)$ (for X = F, Cl, Br, and I) were optimized at the MP2/aug-cc-pVTZ level within the resolution-of-identity approximation. (For bromine and iodine, the corresponding aug-cc-pVTZ-PP basis sets were used along with the eponymous effective core potentials, replacing 10 electrons on Br and 28 electrons on I.) Selected distances and angles for these optimized geometries are listed in Table 1. A one-dimensional reaction coordinate was optimized by constraining the angle θ_{XOH} (Figure 1), relaxing all other degrees of freedom, again at the MP2/aug-cc-pVTZ(-PP) level. Potential energy profiles along this optimized coordinate will be called "relaxed" scans of θ_{XOH}, as we will also consider some "unrelaxed" scans in which the H_2O geometry is fixed. Benchmark interaction energies were computed at the CCSD(T)/aug-cc-pVQZ(-PP) level. Core orbitals for F, Cl, and O were frozen (uncorrelated) in both the MP2 and the CCSD(T) calculations. For Br^- and I^-, all 26 valence electrons were correlated.

Counterpoise corrections are not included in any of the CCSD(T) calculations reported here, which mainly serve to validate the quality of the SAPT energetics that are used for the energy decomposition analysis. (Note that SAPT computes the interaction energy E_{int} directly, rather than by energy difference, so is inherently free of basis-set superposition error.) Interaction energies for $F^-(H_2O)$ computed at the CCSD(T)/aug-cc-pVTZ level are within 0.1 kcal/mol of CCSD(T)/aug-cc-pVQZ values, for both the hydrogen-bonded geometry and the C_{2v} saddle point. Probative counterpoise corrections evaluated at the CCSD(T)/aug-cc-pVQZ level reduce E_{int} for $F^-(H_2O)$ by 0.6 kcal/mol at the hydrogen-bonded geometry and by 0.3 kcal/mol at the saddle

point, while the corresponding corrections for $Cl^-(H_2O)$ are both <0.4 kcal/mol. As noted in Section 3.A below, comparison to other benchmarks in the literature suggests that basis-set effects may be somewhat larger for Br^- and I^- as compared to F^- and Cl^-; nevertheless, the trends that we observe moving down the halide group suggest that our calculations are sufficient for the purpose at hand.

2.B. SAPT Methodology. Energy decomposition analysis was performed at the level of second-order SAPT based on Hartree–Fock wave functions for the monomers, a method commonly known as SAPT0.[39,50] This method is known to overestimate dispersion in the basis-set limit,[51,52] yet at the same time the dispersion energy converges more slowly to that limit as compared to the other energy components, because dispersion depends on monomer polarizabilities. SAPT0 calculations reported here use the partially augmented jun-cc-pVDZ basis set,[53] which represents a compromise that yields SAPT0 results in reasonable agreement with higher-level (partial third-order) SAPT, and it is thus in reasonable agreement with CCSD(T).[50] Given the importance of induction in ion–water complexes,[54] we include a "δE_{HF}" correction to the SAPT0 interaction energy,[39] in which a counterpoise-corrected dimer Hartree–Fock calculation is used to estimate infinite-order induction. Counterpoise correction is an attempt to avoid introducing basis-set superposition error, which is otherwise absent in the SAPT formalism.

Energy decomposition analysis is therefore performed at the level of SAPT0 + δE_{HF}/jun-cc-pVDZ. Despite its reliance on a compromise basis set, interaction energies for the $X^-(H_2O)$ systems are in reasonable agreement with results from variants of the SAPT(KS) method,[41,43,55−61] in which Kohn–Sham (KS) determinants are used in place of monomer wave functions. Table S1 reports CCSD(T), SAPT0, and XSAPT + MBD results, where the latter denotes a recently developed variant that includes self-consistent charge embedding[61] and many-body dispersion (MBD).[60] Both of the SAPT-based methods predict similar interaction energies for $X^-(H_2O)$ complexes, and while XSAPT + MBD values for the C_{2v} barrier height are slightly more accurate as compared to CCSD(T) benchmarks, the improvement is <1 kcal/mol for each of X = F, Cl, and Br. As such, we will perform SAPT analysis at the older and more thoroughly vetted SAPT0 level of theory. Further discussion of the energetics, including comparison to CCSD(T) benchmarks, is deferred to Section 3.

At the SAPT0 + δE_{HF} level of theory, the interaction energy is naturally partitioned according to[41]

$$E_{int} = E_{elst}^{(1)} + E_{exch}^{(1)} + E_{ind}^{(2)} + E_{exch\text{-}ind}^{(2)} + E_{disp}^{(2)} + E_{exch\text{-}disp}^{(2)}$$
$$+ \delta E_{HF}. \tag{1}$$

We will group together the second-order dispersion and exchange-dispersion energies, and simply call the result "dispersion":

$$E_{disp} = E_{disp}^{(2)} + E_{exch\text{-}disp}^{(2)} \tag{2}$$

Furthermore, we identify $E_{elst} \equiv E_{elst}^{(1)}$ and $E_{exch} \equiv E_{exch}^{(1)}$ as the electrostatic and exchange energies, respectively. It is worth explicating the former, which is

$$E_{elst} = \int d\mathbf{r}_1 \int d\mathbf{r}_2 \frac{\rho_A^0(\mathbf{r}_1)\rho_B^0(\mathbf{r}_2)}{\|\mathbf{r}_1 - \mathbf{r}_2\|} \tag{3}$$

where $\rho_A^0(\mathbf{r})$ and $\rho_B^0(\mathbf{r})$ are the isolated monomer densities, corresponding to X^- and H_2O in the present work. At the SAPT0 level, E_{elst} is simply classical electrostatics based on isolated-monomer charge densities (including both nuclei and electrons), computed at the Hartree–Fock level.

The induction energy requires more discussion. Within the SAPT0 formalism, it is natural to define

$$E_{ind} = E_{ind}^{(2)} + E_{exch\text{-}ind}^{(2)} + \delta E_{HF} \tag{4}$$

as the total induction energy. As discussed in Section 1, anything resembling CT is contained within E_{ind}, which might more correctly be called the "polarization + CT" energy.[62] To separate these two effects, we use a version of the SAPT + cDFT method described previously.[43−45] Briefly, the cDFT procedure[48] is used to assemble the dimer A···B in a manner that constrains the charge density $\rho_A(\mathbf{r})$ to integrate to an integer number of electrons. The monomer densities $\rho_A(\mathbf{r})$ and $\rho_B(\mathbf{r})$ can distort as the monomers polarize one another, but CT is turned off in a well-defined way. The energy lowering upon subsequent lifting of the charge constraint is taken to define E_{CT}. Unlike some other definitions of E_{CT}, this one is quite stable with respect to changes in basis set, including large correlation-consistent basis sets.[43] We then subtract E_{CT} from the induction energy defined in eq 4, with the difference taken to define the "true" (CT-free) induction energy. To avoid confusion, we will refer to the latter quantity as the polarization energy:

$$E_{pol} = E_{ind} - E_{CT} \tag{5}$$

(This nomenclature is consistent with other energy decomposition analyses that attempt to separate polarization from CT.) Technically, the cDFT calculations performed in the present work are constrained *Hartree–Fock* calculations, consistent with the monomer wave functions in SAPT0, but the procedure is fully generalizable to SAPT(KS) calculations. Hartree–Fock theory can thus be considered a special case.

The cDFT procedure requires an algorithm to determine the number of electrons on a given monomer.[48] In previous SAPT0 + cDFT calculations reported by our group,[43] we used Becke's multicenter numerical integration algorithm for this purpose,[63] as that method was designed to partition the total integral of a given function (the supramolecular charge density, in the present case) into atomic contributions. Becke's scheme is essentially a smooth version of the Voronoi procedure,[64] and it partitions the density into atomic contributions based strictly on the positions of the nuclei. Since the publication of our earlier SAPT + cDFT algorithm,[43] however, we discovered that the Becke populations are quite sensitive to the presence or absence of the "atomic size adjustments" that are described in ref 63. These corrections use empirical atomic radii in order to adjust the partition of space into Voronoi polyhedra (representing atomic cells). They are included by default in the cDFT algorithm that is implemented in the NWChem program,[65] but not in Q-Chem's implementation of cDFT. We have added these corrections as part of the present work, and we find that they are necessary in order to avoid negative charges on hydrogen atoms. This suggests that the atomic size corrections are probably important when cDFT is used to study hydrogen- or proton-transfer reactions, using cDFT-based nonorthogonal configuration interaction.[48,66]

In the context of SAPT + cDFT, however, the use of fragment-based Hirshfeld partitioning of $\rho(\mathbf{r})$ leads to more
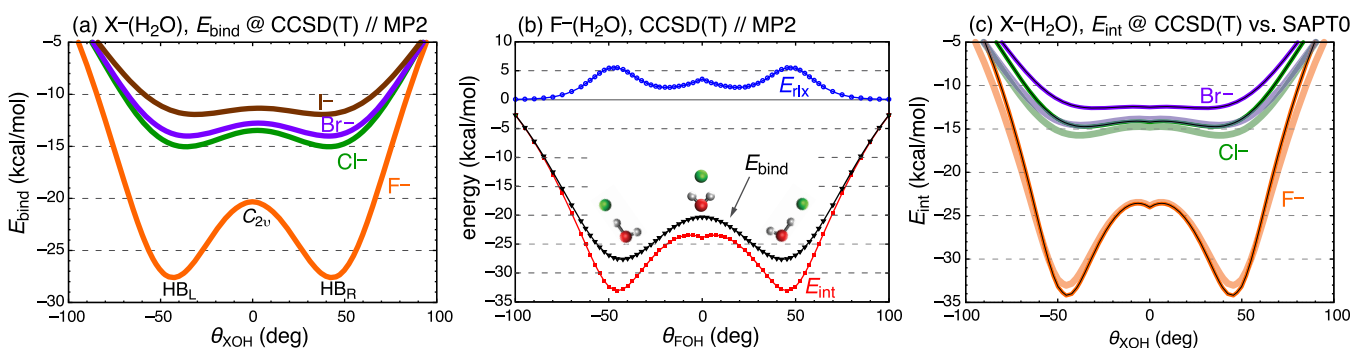
Figure 2. Relaxed potential energy scans along θ_{XOH} for $X^-(H_2O)$: (a) CCSD(T) binding energies for all four $X^-(H_2O)$ complexes; (b) CCSD(T) binding energy ($E_{bind} = E_{int} + E_{rlx}$), interaction energy ($E_{int}$), and H_2O relaxation energy (E_{rlx}) for $F^-(H_2O)$; and (c) comparison of SAPT interaction energies (opaque colors) and CCSD(T) values (translucent colors) for all four complexes. Geometries were optimized at the MP2/aug-cc-pVTZ(-PP) level with θ_{XOH} fixed but all other degrees of freedom relaxed. Angular scans were performed in increments $\Delta\theta_{XOH} = 2.5°$ for $|\theta_{XOH}| \leq 65.0°$ and $\Delta\theta_{XOH} = 5.0°$ for larger angles. Ball-and-stick models in part b depict the asymmetry in the O−H bond lengths that arise in hydrogen-bonded geometries.

Table 2. Energies (in kcal/mol) for $X^-(H_2O)$

| | hydrogen-bonded minimum | | | C_{2v} saddle point | | | ΔE^a | | |
| | CCSD(T)[b] | | SAPT0[c] | CCSD(T)[b] | | SAPT0[c] | CCSD(T)[b] | | SAPT0[c] |
X	E_{bind}	E_{int}	E_{int}	E_{bind}	E_{int}	E_{int}	E_{bind}	E_{int}	E_{int}
F	−27.6	−32.9	−34.2	−20.3	−23.8	−24.0	7.3	9.1	10.2
Cl	−15.0	−15.7	−14.8	−13.5	−14.8	−14.2	1.5	0.9	0.6
Br	−14.0	−14.6	−12.6	−12.8	−13.9	−12.5	1.2	0.7	0.1
I	−11.9	−12.3	—	−11.3	−12.2	—	0.6	0.1	—

$^a\Delta E = E(C_{2v}) - E(\text{H-bond})$. ^{b}aug-cc-pVQZ(-PP) basis with a frozen core for F, Cl, and O, and an effective core potential for Br and I. ^{c}All-electron SAPT0 + δE_{HF}/jun-cc-pVDZ.

consistent results as compared to the use of Becke partitioning.[44] The Hirshfeld (or "stockholder") approach to population analysis[67] is often used to define an atom in a molecule,[68−70] but is applied here to monomers A and B of the noncovalent A···B complex, as in other recent applications of cDFT.[44,71] The number of electrons on monomer A,

$$N_A = \int w_A(\mathbf{r})\rho(\mathbf{r})\,d\mathbf{r} \tag{6}$$

is defined by the weight function

$$w_A(\mathbf{r}) = \frac{\rho_A^0(\mathbf{r})}{\rho_A^0(\mathbf{r}) + \rho_B^0(\mathbf{r})} \tag{7}$$

The denominator in eq 7 is a superposition of isolated-monomer densities, which is sometimes called the "promolecule" density for the A···B complex.[48] This form of population analysis weights the point $\mathbf{r}$ in three-dimensional space according to what fraction of the promolecule density comes from each monomer, with "dividends" (from the supramolecular density) paid out in proportion to "investment" (in the promolecule density). Perhaps more importantly, it can be shown that the Hirshfeld promolecular densities are the ones that best resembles isolated-monomer densities, in an information-theoretical sense.[68−70] Note also that the fragment-based approach removes any ambiguity regarding the definition of Hirshfeld populations for charged subsystems, a topic of considerable discussion when it comes to the Hirshfeld definition of an atom in a molecule,[72,73] leading to various iterative schemes.[72−75] These are unnecessary in the present context.

Fragment-based Hirshfeld analysis has been implemented in Q-Chem as part of the present work and is used in all of the SAPT + cDFT calculations reported herein. The SG-3 quadrature grid[76] is used to integrate eq 6 and related charge constraints. Tests for $F^-(H_2O)$ demonstrate that E_{CT} changes by <0.2 kcal/mol when a benchmark-quality Euler−Maclaurin−Lebedev grid (with $N_r = 250$ and $N_\Omega = 1202$) is employed instead. All SAPT + cDFT calculations are performed within a spin-restricted formalism, using both charge and spin constraints for the cDFT calculations such that the fragments that define the CT-free reference state remain spin-restricted as well.

3. RESULTS AND DISCUSSION

3.A. Benchmarks. For a noncovalent complex A···B, we define the interaction energy using monomer geometries corresponding to the supramolecular complex:

$$E_{int}^{A\cdots B}(\mathbf{R}) = E_{AB}(\mathbf{R}) - E_A(\mathbf{R}) - E_B(\mathbf{R}) \tag{8}$$

This is consistent with the SAPT definition of E_{int} in eq 1. On the other hand, the *binding* energy of A···B is defined as

$$E_{bind}^{A\cdots B}(\mathbf{R}) = E_{int}(\mathbf{R}) + E_{rlx}^A(\mathbf{R}) + E_{rlx}^B(\mathbf{R}) \tag{9}$$

and includes the relaxation energies of the monomers,

$$E_{rlx}^M(\mathbf{R}) = E^M(\mathbf{R}) - E^M(\mathbf{R}_0) \tag{10}$$

for M = A or B, with $\mathbf{R}_0$ indicating the relaxed coordinates of isolated monomer M. For $X^-(H_2O)$, there is no relaxation energy for X^-.

CCSD(T) binding energy profiles $E_{bind}(\theta_{XOH})$ along the relaxed coordinate θ_{XOH} are plotted in Figure 2a for $X^-(H_2O)$

with X = F, Cl, Br, and I. Each is characterized by a saddle point at the C_{2v} geometry, separating symmetric hydrogen-bonded minima. Geometric parameters for these structures are listed in Table 1, and their relative energies are provided in Table 2.

CCSD(T) binding energies for these same complexes have been previously reported,[77] where the results were extrapolated to the basis-set limit using explicitly correlated CCSD(T)-F12b[78]/aug-cc-pVNZ calculations (N = T, Q). Values of E_{bind} reported in the present work for $F^-(H_2O)$ and $Cl^-(H_2O)$ differ from these previous benchmarks by ≤0.2 kcal/mol. For $Br^-(H_2O)$ and $I^-(H_2O)$, however, the binding energies reported here are 1.2 and 1.3 kcal/mol larger, respectively, than those reported in ref 77. Although some systematic errors in CCSD(T)-F12b basis-set extrapolations have been noted,[79−81] the binding energies computed in ref 77 are more consistent with the experimental dissociation energy of $I^-(H_2O)$, estimated at 3200−3500 cm^{-1} (9.1−10.0 kcal/mol).[37,82] This minor discrepancy poses no serious problem, as the present work is focused on understanding the physical nature of the halide−water interaction, for which we rely on SAPT calculations.

According to our CCSD(T) calculations, the HB → C_{2v} barrier height along $E_{bind}(\theta_{XOH})$ is ΔE = 7.3 kcal/mol for $F^-(H_2O)$ but $\Delta E \leq 1.5$ kcal/mol for the larger halides. These barriers are in reasonable agreement with previous theoretical estimates,[29,31,33−35] although the previous estimates are mostly based on lower levels of theory as compared to the calculations reported here. An exception is a potential surface for $F^-(H_2O)$ developed at the CCSD(T)-F12a/cc-pCVTZ-F12 level,[35] which affords a barrier height ΔE = 7.15 kcal/mol that agrees quite well with our result. For the larger halides, the barriers are much smaller. Nevertheless, in microhydrated $X^-(H_2O)_n$ clusters, the ion binding motif nearly always involves a single O−H moiety per water molecule, at least at T = 0 K.[6−11] This includes a recent study for X = Br, I, and At clusters with $n \leq 6$, which found exclusively one-coordinate structures.[83] A few two-coordinate structures for $I^-(H_2O)_n$ have been reported.[84]

The qualitative analysis in Section 3.B will focus on E_{int} more so than E_{bind}. The former is defined as the energy required to separate the monomers in a "vertical" fashion (fixing the H_2O geometry), thus the difference $E_{bind} - E_{int} = E_{rlx}$ is the H_2O relaxation energy (eq 9). All three quantities are plotted for $F^-(H_2O)$ in Figure 2b. Near the hydrogen-bonded minima, which are characterized by quasi-linear hydrogen bond angles $\theta(X\cdots HO) \geq 164.5°$ (Table 1), the H_2O relaxation energy is relatively large, as a result of asymmetric O−H bond lengths that we will ultimately ascribe to a CT process, $X^- \rightarrow \sigma^*_{OH}$. Population of the antibonding σ^* orbital for O−H_1 lengthens this bond (as compared to O−H_2) at the hydrogen-bonded $X^-\cdots H_1OH_2$ geometry, whereas $r(OH_2)$ remains similar to the (symmetric) O−H bond lengths at the C_{2v} geometry.

An interesting feature of the CCSD(T) energy profiles $E_{int}(\theta_{XOH})$ is a cusp at the C_{2v} geometry ($\theta_{XOH} = 0$). This is evident for $F^-(H_2O)$ in Figure 2b but is present for all four halides, and is a feature of SAPT interaction energy profiles as well. The H_2O relaxation energy also exhibits a cusp (Figure 2b), which precisely cancels the cusp in $E_{int}(\theta_{XOH})$, such that $E_{bind}(\theta_{XOH})$ is smooth at $\theta_{XOH} = 0$. If the SAPT interaction energy E_{int} is combined with the CCSD(T) relaxation energy E_{rlx} to define $E_{bind} = E_{int} + E_{rlx}$, the cusp also cancels and affords a binding energy profile $E_{bind}(\theta_{XOH})$ that is differentiable at $\theta_{XOH} = 0$; see Figure S1.

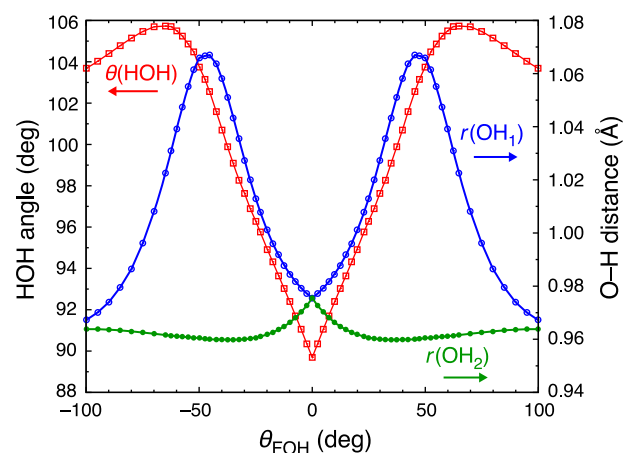**Figure 3.** Geometric parameters of $F^-(H_2O)$ along the relaxed θ_{XOH} reaction coordinate. The H_2O bond angle is read from the axis on the left and the two O−H bond lengths are read from the axis on the right. The $r(OH_1)$ and $r(OH_2)$ curves exhibit an avoided crossing at $\theta_{XOH} = 0$.

This curious feature turns out to be an artifact of the symmetry of these complexes and in particular the cyclic boundary conditions that accompany θ_{XOH}. Figure 3 plots several geometric parameters of $F^-(H_2O)$ along the relaxed θ_{XOH} pathway, including the H_2O bond angle and both O−H bond lengths. A sharp compression in the bond angle is evident as the system approaches the C_{2v} geometry, which serves to enhance the H_2O dipole moment by 0.234 D (or 12%) in the C_{2v} geometry as compared to its value in the equilibrium geometry of isolated H_2O. The H_2O dipole moment is also larger by 0.155 D in the C_{2v} geometry of $F^-(H_2O)$, as compared to the hydrogen-bonded geometry. (The quoted dipole moments are from the Hartree−Fock monomer wave function for H_2O.) The reason for the cusps becomes evident upon examining the O−H bond lengths, both of which also exhibit cusps at $\theta_{XOH} = 0$. These arise because the longer (hydrogen-bonded) O−H bond trades roles with the shorter (free) O−H moiety at $\theta_{XOH} = 0$. The cusps in $r(OH_1)$ and $r(OH_2)$ that appear as a function of θ_{XOH} are essentially avoided crossings between two diabatic bond-length curves. As usual, molecular point-group symmetry is nothing but a topological trick that small systems play in order to appear more complicated than they otherwise would be, given a higher-dimensional space.

3.B. Energy Decomposition Analysis. The remainder of this work focuses on interaction energies rather than binding energies, and it uses the SAPT0 + δE_{HF}/jun-cc-pVDZ level of theory for energy decomposition analysis. Considering both the C_{2v} saddle point and the hydrogen-bonded minima, CCSD(T) interaction energies for $X^-(H_2O)$ span a range only from −12 to −16 kcal/mol if $F^-(H_2O)$ is excluded; see Table 2. The larger halides (X = Cl, Br, and I) are thus more similar to one another than they are to fluoride. In light of this, our SAPT analysis will focus on a comparison between X = F, Cl, and Br, for which it is possible to use a consistent all-electron basis set, jun-cc-pVDZ.

Figure 2c juxtaposes energy profiles $E_{int}(\theta_{XOH})$ computed with SAPT and CCSD(T), along the relaxed coordinate θ_{XOH}. At their respective hydrogen-bonded minima, the SAPT and CCSD(T) interaction energies differ by ≈1 kcal/mol for both $F^-(H_2O)$ and $Cl^-(H_2O)$, and by ≈2 kcal/mol for $Br^-(H_2O)$.
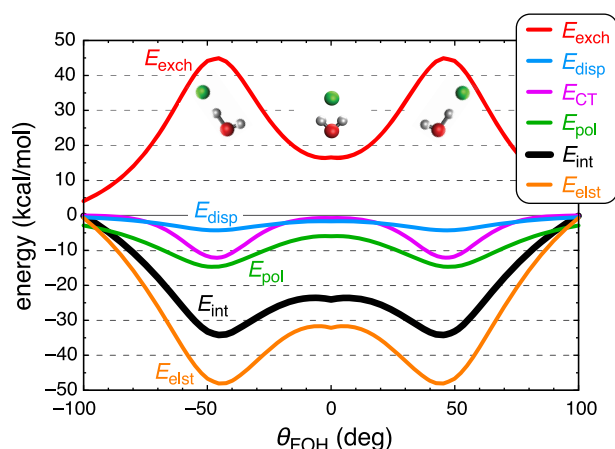
Figure 4. Relaxed scan of θ_{FOH} for $F^-(H_2O)$, illustrating energy components computed at the SAPT0 + δE_{HF}/jun-cc-pVDZ level. Ball-and-stick models show the asymmetry of the O–H bond lengths that emerges in the hydrogen-bonded minima. The sum of the five components equals the total interaction energy, E_{int}.

Differences at the C_{2v} saddle point are smaller still. Comparison to previous benchmarks[77] suggests that our CCSD(T) interaction energies for $Br^-(H_2O)$ and $I^-(H_2O)$ may be slightly larger than complete-basis values, as discussed in Section 3.A, and the SAPT results certainly agree well enough for qualitative and semiquantitative purposes.

Energy components for $F^-(H_2O)$ are plotted in Figure 4 for a relaxed scan along θ_{FOH}, and the corresponding data for $Cl^-(H_2O)$ and $Br^-(H_2O)$ can be found in Figure S2. As a reminder, the decomposition is

$$E_{int} = E_{exch} + E_{elst} + E_{pol} + E_{disp} + E_{CT} \qquad (11)$$

with components that were defined in Section 2.B. Along with electrostatics (E_{elst}), the exchange or Pauli repulsion term E_{exch} is largest in magnitude; both are larger in magnitude than the total interaction energy, E_{int}. Polarization and CT make smaller but still significant contributions. Dispersion plays little role in these systems.

An interesting observation from Figure 4 is that electrostatics favors the hydrogen-bonded geometry over the dipolar geometry, a reversal of the textbook electrostatics picture. There is no paradox in this observation, which adds to other recent examples (in the context of π-stacking[85–88]) demonstrating that low-order multipoles qualitatively fail to describe

electrostatic interactions at distances characteristic of the equilibrium geometries of van der Waals complexes. At these close-contact distances, so-called "charge penetration" effects[42,88] generally result in attractive electrostatic interactions ($E_{elst} < 0$),[85–89] even in cases where the leading-order multipoles suggest electrostatic repulsion at larger distances. This phenomenon is well-documented in SAPT calculations yet does not seem to be widely appreciated. Note also that *charge penetration* is distinct from *charge transfer*.[88] The former describes deviations from multipolar electrostatics engendered by interpenetration of the monomer densities, whereas the latter arises from density relaxation in the presence of the other monomer. According to eq 3, the electrostatics term does not include any density relaxation at all, as it is computed using isolated-monomer densities.

The origins of short-range electrostatic attraction are entirely classical, in accordance with the classical formula in eq 3. It is helpful to recall a theorem in classical electrostatics stating that the electrostatic repulsion between two distributions of like charge (electron densities, for example) is always smaller, as those charge clouds approach one another and begin to interpenetrate, than is the Coulomb interaction between two point charges that concentrate the entirety of either distribution at the respective centers of charge.[62] As a result, the electrostatic interaction at typical van der Waals contact distances is dominated by the fact that electrons on molecule A gain access to the nuclei on molecule B (and *vice versa*), which has a stabilizing effect, while the Coulomb repulsion caused by interpenetration of the two electron clouds is relatively small, with the net effect that $E_{elst} < 0$. Only at long-range, where the nuclei of each molecule are better screened by their respective electron distributions, is a multipolar picture recovered.

In the case of $X^-(H_2O)$, the leading-order multipolar interaction (charge–dipole) is attractive, so $E_{elst} < 0$ at both short range and long range. Nevertheless, at close-contact distances even the classical electrostatics term favors the hydrogen-bonded geometry over the dipolar coordination motif. It is worth noting that the total H_2O dipole moment is larger in the C_{2v} geometry of $F^-(H_2O)$ only by 7% (or 0.155 D) as compared to its value in the hydrogen-bonded geometry, although the orientation of the dipole moment vector $\boldsymbol{\mu}(H_2O)$ shifts slightly as a function of the angle θ_{FOH}, as asymmetry develops between the two O–H bond lengths. At the hydrogen-bonded geometry ($\theta_{FOH} = 44.9°$), the projection of $\boldsymbol{\mu}(H_2O)$ onto $\mathbf{r}(OH_1)$ is 19% larger than its projection onto
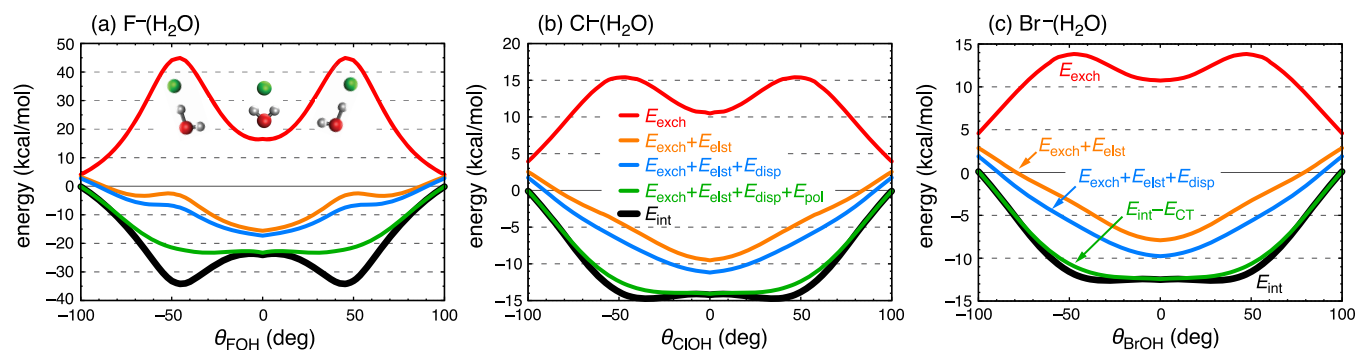
Figure 5. Relaxed scans of θ_{XOH} for (a) $F^-(H_2O)$, (b) $Cl^-(H_2O)$, and (c) $Br^-(H_2O)$, illustrating sequential construction of the SAPT0 + δE_{HF} interaction potential, $E_{int}(\theta_{XOH})$. In each panel, the full interaction potential (E_{int}) is assembled term-by-term, as indicated by the common legend that is shown in part b. Ball-and-stick models in part a show the asymmetry in the O–H bond lengths that develops in hydrogen-bonded geometries. The CT energy is not included here but can be surmised from the difference between E_{int} and $E_{exch} + E_{elst} + E_{disp} + E_{pol}$.

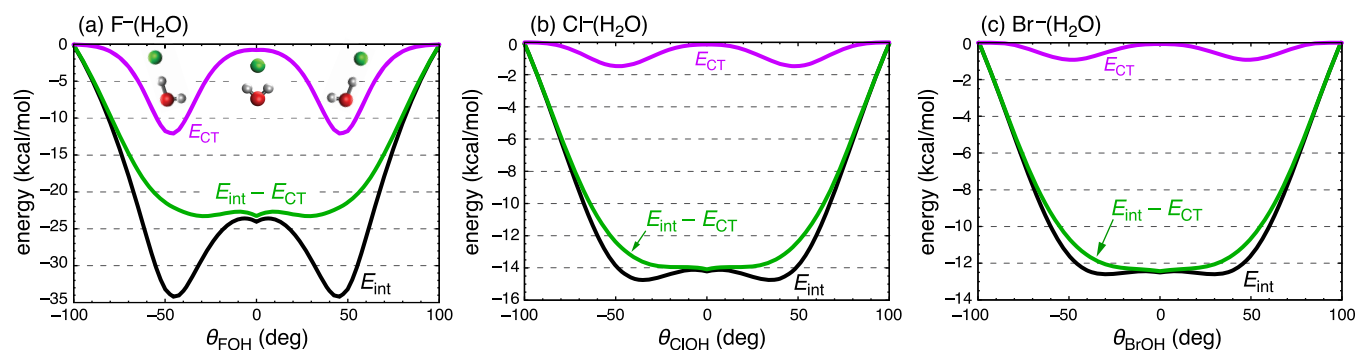**Figure 6.** Relaxed scans of θ_{XOH} for (a) $F^-(H_2O)$, (b) $Cl^-(H_2O)$, and (c) $Br^-(H_2O)$, illustrating the effect of CT on the interaction energy. The quantities plotted include $E_{int}(\theta_{XOH})$ and $E_{CT}(\theta_{XOH})$ from the SAPT0 + δE_{HF} calculations, along with their difference, $E_{int} - E_{CT}$. Ball-and-stick models in part a illustrate the asymmetry of the two O–H bond lengths at hydrogen-bonded geometries. The minimum on the CT-free energy profile lies at the C_{2v} geometry in each case, although the potential $E_{int} - E_{CT}$ is quite flat within the angle subtended by the two O–H bond vectors.

$r(OH_2)$ even though the magnitude of the total H_2O dipole moment is smaller than it is in the C_{2v} geometry. These asymmetric projections result from the lengthening of O–H_1 relative to O–H_2 and not from polarization, which is a separate effect.

These relatively small distortions of $\boldsymbol{\mu}(H_2O)$, as a function of geometry along the relaxed θ_{XOH} coordinate, are insufficient to rationalize the *electrostatic* preference for hydrogen bonding in terms of low-order, single-center multipoles for H_2O. In classical force fields, Thole-type[90] distributed polarizability models have long been used to sidestep the short-range inadequacies of the single-center multipole expansion.[91−93] These have been developed in particular both for water itself[94−98] and for ion–water interactions,[77,99−104] and they are capable of describing single-coordinate hydrogen bonds in $X^-(H_2O)$.[104] The textbook dipolar picture,[12,13] however, is inadequate even to describe the classical electrostatics.

While electrostatics favors the hydrogen-bonded geometry, the Pauli repulsion is also larger in that configuration (see Figure 4), because $r(XH_1)$ is significantly shorter as compared to the two symmetric $r(XH)$ distances that characterize the C_{2v} geometry (Table 1). The difference in the value of $r(XH_1)$ at the two geometries ranges from 0.63 Å for X = F to 0.39 Å for X = I. This sets up a competition between steric repulsion and electrostatics.

In an effort to understand the molecular physics behind why the hydrogen-bonded geometry emerges as the minimum-energy structure, Figure 5 provides a sequential construction of the interaction potentials $E_{int}(\theta_{XOH})$ for X = F, Cl, and Br, component-by-component according to eq 11. (Results of a different sequential construction, in which the energy components are added together in a different order, can be found in Figure S3.) Summing the two largest components, $E_{exch} + E_{elst}$, one obtains in each case an energy profile whose global minimum resides at the C_{2v} geometry. This potential does have some additional structure in the case of $F^-(H_2O)$ but those features are absent for the larger halides, for which $E_{exch} + E_{elst}$ exhibits only a single minimum at the dipolar C_{2v} geometry. For the halides larger than F^-, the textbook picture adequately describes $E_{exch} + E_{elst}$, though it is interesting to note that even in these cases, dipolar coordination is not driven by electrostatics alone and can only be understood in the presence of Pauli repulsion. (The same conclusion has been reached previously regarding the geometries of halogen-bonded complexes.[105]) Electrostatic attraction is maximized

in the hydrogen-bonded configuration (see Figures 4 and S2), and the preference for the dipolar motif emerges only when E_{exch} is added to E_{elst}. Electrostatics plus finite atomic size is the minimal sensible starting point for understanding the halide–water interaction, but this minimalist model incorrectly favors dipolar coordination for each of the halide ions, including fluoride.

The dispersion energy is not isomer-selective for these systems and the addition of E_{disp} to $E_{exch} + E_{elst}$ results in a small shift but does not change the shape of the energy profile, leaving the dipolar structure as the global minimum of $E_{exch} + E_{elst} + E_{disp}$. On the other hand, the CT-free polarization energy (E_{pol}) favors the hydrogen-bonded configuration. Its addition defines the CT-free SAPT interaction energy, $E_{int} - E_{CT}$. For convenient future reference, we note two trivial rearrangements of eq 11:

$$E_{int} - E_{CT} = E_{exch} + E_{elst} + E_{disp} + E_{pol} \quad (12a)$$

$$E_{int} - E_{pol} = E_{exch} + E_{elst} + E_{disp} + E_{CT} \quad (12b)$$

These will be used in order to distinguish the role of E_{pol} from that of E_{CT}.

The potential $E_{int} - E_{CT}$ is plotted for the various $X^-(H_2O)$ complexes in Figure 6. It is quite flat in the vicinity of the C_{2v} geometry, and indeed for any value of θ_{XOH} that lies within the angle subtended by the two O–H bond vectors, i.e., for $|\theta_{XOH}| \lesssim \theta(H_2O)/2$. As is evident in Figure 5, polarization eliminates the strong preference for the dipolar binding motif; however, the $E_{int} - E_{CT}$ plots in Figure 6 demonstrate that polarization alone is insufficient to create a distinct hydrogen-bonded structure. For that, CT is required.

As others have pointed out,[106] the IUPAC definition of the hydrogen bond[107] suggests that an X···H–O angle approaching 180° is an essential aspect, yet it does not provide a rationale. Attempts have been made to explain this linearity in terms of topological properties of the electron density,[106,108] yet simple orbital-overlap arguments remain compelling.[22] For the systems considered here, examination of CT-free interaction energy profiles provides a clear explanation. Plots of $E_{int} - E_{CT}$ along the relaxed coordinate connecting the C_{2v} and hydrogen-bonded geometries demonstrate convincingly that the CT term alone drives the conformational preference for quasi-linear hydrogen bonds. As the X···O–H angle approaches linearity, E_{CT} turns on sharply and stabilizes the interaction. In contrast, $E_{CT} \approx 0$ for the C_{2v} geometry.
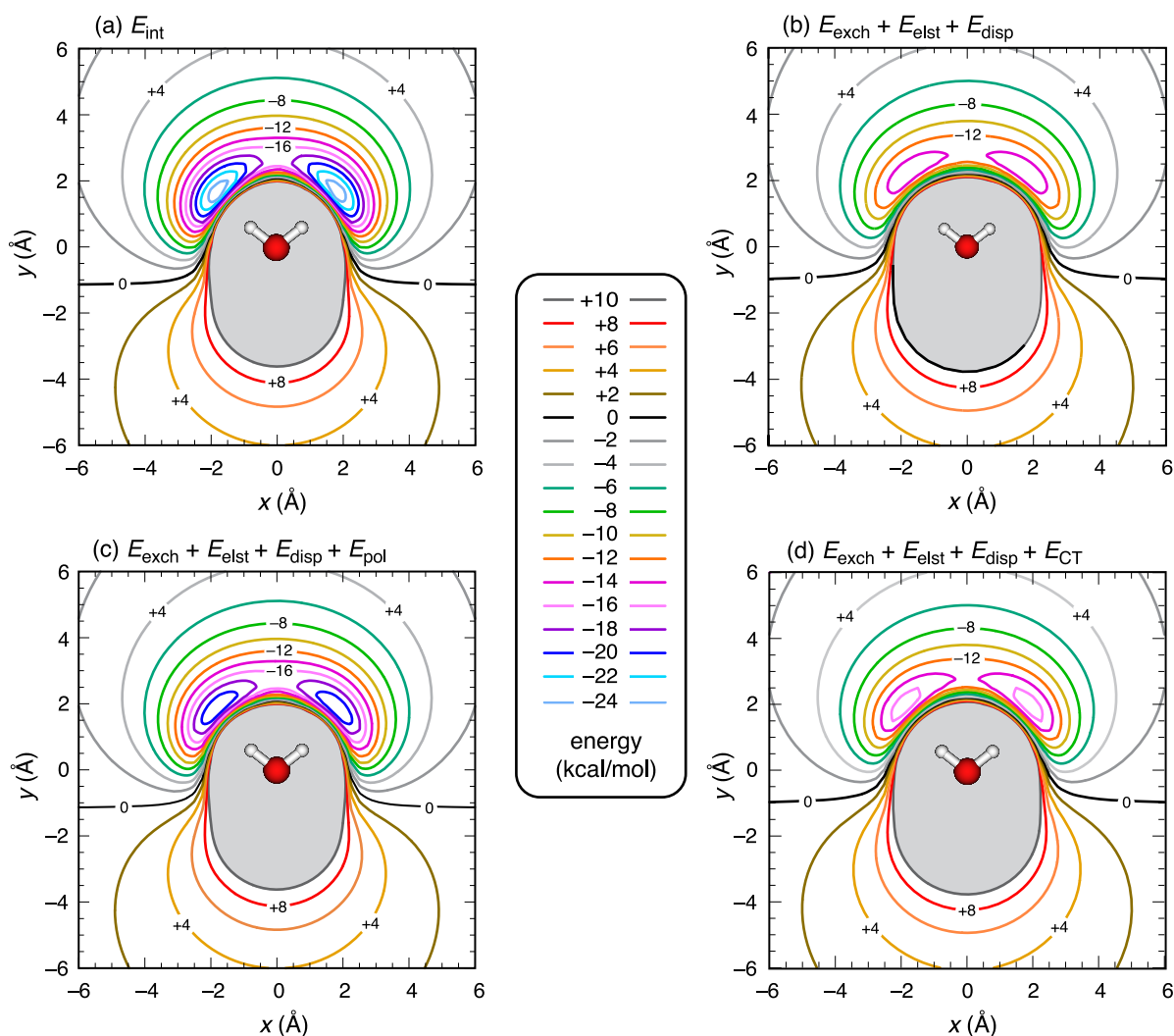
Figure 7. Contour plots of the fluoride−water interaction potential and its sequential construction from SAPT energy components, scanning the position of F⁻ in the plane of a fixed-geometry H_2O molecule. Shown are (a) the full interaction potential, E_{int}; (b) $E_{int} - E_{ind} = E_{exch} + E_{elst} + E_{disp}$, where the entirety of the SAPT induction energy ($E_{ind} = E_{pol} + E_{CT}$) has been removed and (for a given F···O distance) is rather flat for $|\theta_{FOH}| \lesssim \theta(H_2O)/2$; (c) $E_{int} - E_{CT}$; and (d) $E_{int} - E_{pol}$. The potentials in parts c and d each include one part of the SAPT induction energy (E_{pol} or E_{CT} but not both), and both potentials exhibit a clear preference for quasi-linear hydrogen bonds. The H_2O geometry is indicated (with oxygen at the coordinate origin) and corresponds to the isolated-monomer geometry optimized at the MP2/aug-cc-pVTZ level. Energy components were computed at the SAPT0 + δE_{HF}/jun-cc-pVDZ level on a grid of points extending to ± 6.0 Å in both x and y, with $\Delta x = 0.25$ Å $= \Delta y$. Regions more repulsive than +10 kcal/mol are shaded in gray.

Note that the manner in which we separate E_{CT} from E_{ind}, based on a charge-constrained self-consistent field (SCF) calculation, is density-based rather than orbital-based. This is intentional, as orbital-based definitions of E_{CT} are typically quite sensitive to the choice of AO basis set, especially for high-quality basis sets where functions centered on one monomer extend significantly onto the other monomer.[43] Despite this density-based definition of E_{CT}, however, the SCF calculation itself is orbital-based, and it is easy to rationalize our observations in terms of molecular orbitals. Specifically, CT turns on as the overlap of the donor orbital (X^- lone pair) and the acceptor orbital (σ_{OH}^*) comes into alignment, at near-linear X···H−O angles. This remains true for $Cl^-(H_2O)$ and $Br^-(H_2O)$ even though the CT energy is much smaller in these cases than it is in $F^-(H_2O)$, befitting the larger size of the ions and the exponential falloff of CT with respect to donor−acceptor distance. Even for the larger halides, however, the CT

term alone is responsible for the double-well nature of the energy profile along the relaxed coordinate θ_{XOH}.

If one plots $E_{bind} - E_{CT}$ rather than $E_{int} - E_{CT}$, by combining the CCSD(T) relaxation energy for H_2O with the SAPT0 + δE_{HF} value of E_{int}, then a very shallow double-minimum potential does emerge even in the absence of CT, as shown in Figure S1. For $F^-(H_2O)$, however, the two symmetric minima in $E_{bind} - E_{CT}$ lie only 1.2 kcal/mol below the C_{2v} saddle point, and the analogous minima for the larger halides are even more shallow. Moreover, the geometries corresponding to these minima on the $E_{bind} - E_{CT}$ surface exhibit significant distortion away from linear hydrogen bonds, e.g., $\theta(F···H_1-O) = 144.5°$, corresponding to $\theta_{XOH} = 22.9°$, and $\theta(Cl···H_1-O) = 147.8°$. These shallow minima result from the H_2O deformation penalty, and in a sense they are deceptive because this deformation is driven by $X^- \rightarrow \sigma_{OH_1}^*$ CT, resulting in lengthening of $r(OH_1)$. This asymmetric distortion would not occur in the absence of CT.

This subtlety does suggest that it might be informative to examine unrelaxed potential energy scans, in which θ_{XOH} is varied for a fixed water geometry and the H_2O deformation penalty is avoided altogether. In the relaxed scans, the water geometry is distorted (with respect to isolated H_2O) in both the hydrogen-bonded geometries, where there is significant asymmetry between the O−H bond lengths, but also in the C_{2v} geometry where the H_2O bond angle is substantially compressed; see Figure 3.

As an alternative, Figure 7a presents a two-dimensional potential surface $E_{int}(x, y)$ for coplanar $F^-(H_2O)$, in which H_2O is fixed at its isolated-monomer geometry while the position of F^- is scanned over the (x, y) plane defined by the water molecule. Deep wells corresponding to hydrogen-bonded minima are evident even in the absence of ion-induced distortion of the H_2O geometry. These wells remain even when E_{CT} is removed (Figure 7c), although they are not as deep because the CT energy is large for hydrogen-bonded configurations but negligible in geometries close to C_{2v} symmetry. That fact alone is significant. From a comparison of the potential with CT (Figure 7a) versus one without it (Figure 7c), and scanning the angle θ_{FOH} while the distance $r(FO)$ is fixed, it is evident that the CT energy goes nearly to zero at the C_{2v} geometry, even when $r(FO)$ is rather short. This confirms that the magnitude of E_{CT} is not strictly distance-related, and reinforces the orbital-based explanation for the sudden amplification of E_{CT} in the vicinity of linear hydrogen bonds.

Next consider the two-dimensional profile of $E_{exch} + E_{elst} + E_{disp}$ (equivalent to $E_{int} - E_{pol} - E_{CT}$) that is plotted in Figure 7b. At the minimum-energy F···O distance of 2.49 Å, symmetric minima develop at $\theta_{FOH} = \pm 27°$ but these lie only 0.6 kcal/mol below the C_{2v} structure at $\theta_{FOH} = 0$. As such, the attractive contours of this potential can *almost* be understood from a charge−dipole point of view, although the contours are largely independent of θ_{FOH} for a given value of $r(FO)$. This means that the electrostatic preference for hydrogen bonds at $|\theta_{FOH}| \approx 45°$ is enough to level out the angular contours so that there is no preference for a C_{2v} geometry corresponding to a linear ion−dipole arrangement. To significantly stabilize the hydrogen bonds and bring them below the C_{2v} geometry, either E_{CT} or E_{pol} is required, as demonstrated by contour plots of $E_{int} - E_{CT}$ (Figure 7c) and $E_{int} - E_{pol}$ (Figure 7d). Unlike the situation described above for relaxed θ_{XOH} scans, in this rigid-water example both E_{pol} and E_{CT} contribute to stabilizing hydrogen-bonded configurations. This complicates the picture, as compared to that discussed above.

To investigate this in more detail, Figure 8a plots one-dimensional cuts through the two-dimensional potentials in Figure 7, scanning θ_{FOH} at a fixed distance $r(FO) = 2.490$ Å corresponding to the global minimum of $E_{int}(x, y)$ in Figure 7a. The one-dimensional potentials that are plotted include the total interaction potential $E_{int}(\theta_{FOH})$ as well as $E_{int} - E_{ind}$, $E_{int} - E_{pol}$, and $E_{int} - E_{CT}$. These are *unrelaxed* scans, so to make contact with the relaxed scans that were discussed above, we plot the latter (in an analogous way) in Figure 8b. In the relaxed scans, the quantity $E_{exch} + E_{elst} + E_{disp}$ strongly favors the C_{2v} geometry whereas for the unrelaxed scans this same potential is essentially flat (varying by <0.6 kcal/mol) within the angle subtended by the two O−H bond vectors.

A similarly flat potential is obtained in the relaxed scans only after the addition of E_{pol}; see the $E_{int} - E_{CT}$ profile in Figure

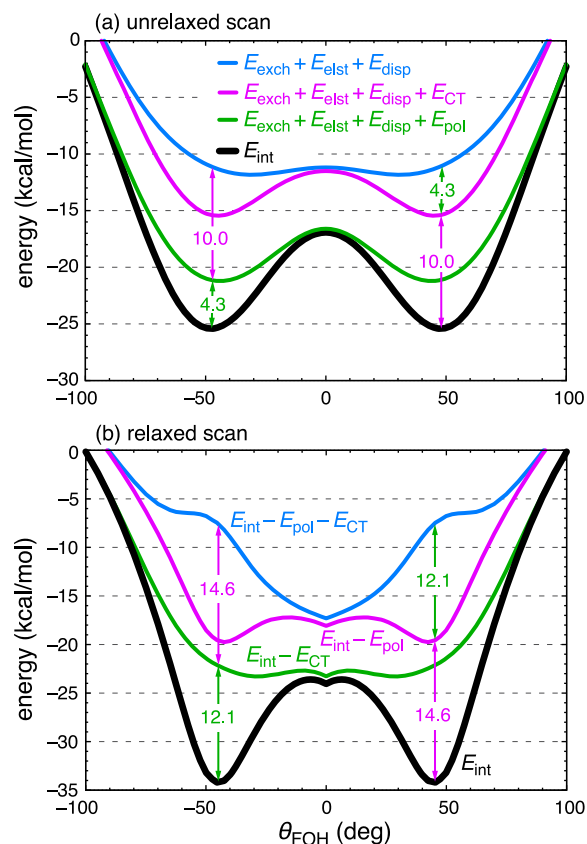**Figure 8.** Energy profiles for $F^-(H_2O)$ along θ_{FOH}. (a) An unrelaxed scan, using the isolated-monomer H_2O geometry and a fixed distance $r(FO) = 2.490$ Å that corresponds to the minimum of $E_{int}(x, y)$ in Figure 7a. (b) A relaxed scan, in which all degrees of freedom except θ_{FOH} are optimized. The $E_{int}(\theta_{FOH})$ profile in part a corresponds to an angular cut through the two-dimensional potential in Figure 7a, whereas E_{int} and $E_{int} - E_{CT}$ in part b are the same as in Figure 6a. The coloring scheme is the same in both panels, and values of E_{CT} and E_{pol} at the hydrogen-bonded minima are indicated.

8b. In light of this comparison, it is now clear that the strong preference for the dipolar binding motif that is exhibited by the sum of electrostatics and finite atomic size ($E_{elst} + E_{exch}$) in the relaxed scans arises entirely from enhancement of the dipole moment due to compression of the H_2O bond angle as the system approaches a C_{2v} geometry. In the absence of such compression (Figure 8a), electrostatics and Pauli repulsion together exhibit essentially no angular preference, so long as $|\theta_{FOH}| \lesssim \theta(H_2O)/2$, corresponding to the strongly attractive region of the potential. Dispersion does not alter this conclusion, leading to the nearly isotropic angular contours in Figure 7b.

Addition of either E_{CT} or E_{pol} to the mix is enough to establish a preference for hydrogen bonding, as demonstrated by one-dimensional plots of $E_{int} - E_{CT}$ and $E_{int} - E_{pol}$ in Figure 8a. Both E_{CT} and E_{pol} stabilize the hydrogen bond, by 4.3 and 10.0 kcal/mol, respectively, at the minimum-energy geometry. Either component is also sufficient to establish a quasi-linear hydrogen bond, as evidenced by the double-well nature of both potentials. Hydrogen bond angles on the $E_{int} - E_{CT}$ surface are $\theta(F···H_1−O) = 167.8°$, for example.

How can one understand the seemingly different role of CT in the relaxed versus unrelaxed angular scans for $F^-(H_2O)$? The answer lies in the geometry of H_2O. In the relaxed scans,

$\theta(H_2O)$ becomes increasingly compressed as the system approaches the C_{2v} geometry, enhancing the H_2O dipole moment such that $E_{exch} + E_{elst}$ strongly favors the dipolar binding motif. Polarization counteracts that tendency just enough to undo the preference for dipolar binding but not enough to stabilize a proper minimum corresponding to hydrogen bonding. For that, CT is required. In the unrelaxed scans, compression of $\theta(H_2O)$ is not allowed and E_{pol} is put to use in stabilizing the hydrogen bond, alongside E_{CT}. Elongation of the hydrogen-bonded O−H bond, driven by anion-to-σ^*_{OH} CT, creates a larger bond dipole in the asymmetric hydrogen-bonded geometry, which in turn facilitates a larger value of E_{pol} than is possible in the rigid-water calculations.

Figure S4 shows the two-dimensional potential surface for $Cl^-(H_2O)$, for a fixed H_2O geometry corresponding to an isolated water monomer, analogous to Figure 7 for $F^-(H_2O)$. In the chloride−water case, the total interaction potential shows only a slight preference for asymmetric hydrogen bonding, with minima at $\theta(Cl\cdots H-O) = 161°$ that are 1.6 kcal/mol below the lowest-energy C_{2v}-symmetric geometry. As compared to $F^-(H_2O)$, the larger size of the ion diminishes the role of CT in the case of $Cl^-(H_2O)$, and for the isolated-water geometry it is E_{pol}, rather than E_{CT}, that drives the asymmetry of the potential in the chloride−water case. Nevertheless, when hydrogen bonding is allowed to distort the H_2O geometry, it is clear that CT drives the (slight) preference for hydrogen bonding (Figure 6b). Since relaxation of the H_2O geometry represents the more realistic scenario for a water molecule in close proximity to the ion, we conclude that CT is the essential element of the quasi-linear hydrogen bond.

3.C. Broader Implications. The notion of a CT component to hydrogen bonding, leading in particular to vibrational frequency shifts, is quite old.[14−22] Even for hydrogen bonds between charge-neutral monomers, most energy decomposition schemes predict at least some role for CT, as indicated by a survey of methods applied to $(H_2O)_2$.[109] Topological indicators developed in the context of Bader's theory of atoms in molecules also suggest a CT component to hydrogen bonding.[83,110,111] Even so, the detailed role of CT in hydrogen bonding has long been debated.[112−116]

The hydrogen bond in $(H_2O)_2$ has been investigated with SAPT-based methods by Stone and co-workers,[114,117] who report no role whatsoever for CT. However, the study in ref 117 used a definition of E_{CT} that provably goes to zero in the complete-basis limit.[43] Using instead a definition based on Misquitta's regularization method,[47] which does not suffer from this defect, Stone obtains $E_{CT} = -0.4$ kcal/mol for $(H_2O)_2$ using SAPT(DFT).[114] For comparison, the same calculation affords $E_{int} = -4.5$ kcal/mol and $E_{elst} = -6.7$ kcal/mol. Comparable results for $(H_2O)_2$ are obtained at the level of theory used here: $E_{CT} = -0.45$ kcal/mol, out of a total interaction energy $E_{int} = -5.18$ kcal/mol and in comparison to $E_{elst} = -8.93$ kcal/mol. As such, our own analysis suggests that CT constitutes <10% of the total interaction energy in $(H_2O)_2$, which was the rationale for Stone's dismissal of the significance of CT in the water−water hydrogen bond. However, results presented for $X^-(H_2O)$ in Section 3.B demonstrate that the CT term can have a dramatic effect on conformational preferences. CT constitutes an energetically small contribution, yet one whose presence is crucial to the properties of what we understand as a hydrogen bond, including the incipient covalency that imparts a strong preference for quasi-linear hydrogen bond angles.

Returning to the topic of ion−water hydrogen bonds, Johnson and co-workers[2,3,38] have measured gas-phase vibrational spectra for binary complexes of H_2O with a variety of oxyanions, in addition to the halide-water complexes. These experiments demonstrate a clear correlation between the vibrational redshift of the hydrogen-bonded O−H stretching mode and the proton affinity of the anion, signifying a role for the proton-transferred diabatic state XH + OH^-.[2,27] The largest vibrational redshift (at almost 3000 cm^{-1}) is observed in the case of $OH^-(H_2O)$, versus ≈2000 cm^{-1} for $F^-(H_2O)$ and <600 cm^{-1} for the other binary halide−water complexes.[3] Our calculations confirm that the ordering of these shifts is consistent with the magnitude of E_{CT} computed by the method described herein. At the minimum-energy geometry of the $OH^-(H_2O)$ complex, for example, we obtain $E_{CT} = -12.8$ kcal/mol, as compared to $E_{CT} = -11.7$ kcal/mol for $F^-(H_2O)$ and $E_{CT} = -1.3$ kcal/mol for $Cl^-(H_2O)$. For $NO_2^-(H_2O)$, where the redshift is ≈700 cm^{-1},[2] we obtain $E_{CT} = -1.3$ kcal/mol. While the proton affinity serves as a useful thermodynamic proxy for the vibrational redshifts,[2,3,38] it seems that CT energies are also useful in this capacity.

Work by others,[28] on both $(H_2O)_2$ and $Cl^-(H_2O)$, has shown that the vibrational redshift in the hydrogen-bonded O−H stretch largely disappears when frequencies are computed on a potential energy surface from which the CT energy has been removed. Restricting the calculation to disallow CT also has the effect of significantly diminishing the intensity of the hydrogen-bonded O−H stretch, bringing it closer to that of the free O−H moiety.[28] This observation is fully consistent with the idea of a "charge sloshing" mechanism as the origin of the intense vibrational transitions associated with anion−water hydrogen bonds.[3,26,27] The strong angular dependence of the CT term that is documented in the present work suggests a possible mechanism for electrical anharmonicity in the vibrational spectra of $X^-(H_2O)$ complexes,[3,31,37] when stretch−bend coupling is considered.

4. CONCLUSIONS

We have introduced a modified version of the SAPT + cDFT energy decomposition procedure described in a previous work.[43] The present version uses cDFT with fragment-based Hirshfeld population analysis, in order to separate the SAPT induction energy into a CT component and a CT-free polarization energy. By means of this technique, we have explored the origins of the double-well potential in halide−water complexes $X^-(H_2O)$ and, in particular, the conformational preference for hydrogen bonding over coordination of X^- at the positive end of the H_2O dipole moment vector.

Our analysis demonstrates that CT provides the driving force for formation of quasi-linear halide−water hydrogen bonds. An $X\cdots H-O$ angle close to 180° is a defining characteristic of the hydrogen bond,[107] so it is notable that when the CT energy is removed, the potential energy minima in $X^-(H_2O)$ that correspond to quasi-linear hydrogen bonds disappear, along optimized reaction coordinates θ_{XOH}. What remains of the interaction potential $(E_{int} - E_{CT})$ exhibits a single minimum at the C_{2v} "dipolar" geometry. This is true for the strongly interacting $F^-(H_2O)$ system but also for the larger halides, despite the fact that the CT energy is a relatively small part of the total interaction energy, significantly smaller than the electrostatic energy.

The picture is somewhat more nuanced when one considers the interaction of F^- with a rigid H_2O monomer, i.e., when the

geometry is not relaxed at each position of the ion. In that case, both E_{CT} and E_{pol} contribute to stabilizing the hydrogen-bonded geometry with respect to the dipolar coordination motif. When the geometry of the complex is relaxed in the presence of the ion, scanning θ_{FOH} to generate the characteristic double well, polarization is required to counteract the effects of an enhanced H_2O dipole due to compression of water's bond angle in the vicinity of the C_{2v} geometry of the ion–water complex. In a frozen-monomer calculation, there is no such competing effect, and the classical picture (corresponding to the potential $E_{exch} + E_{elst}$) is already ambivalent as to the formation of hydrogen bonds versus dipolar binding.

In attempting to define what constitutes a hydrogen bond, it has been asserted that "no single physical force can be attributed to hydrogen bonding".[14] Some theoretical surveys have pointed to the dominant role of electrostatic interactions.[22] Our analysis, however, reveals that CT makes a qualitatively important contribution to the geometry of halide–water hydrogen bonds. Despite the fact that the CT energy in $X^-(H_2O)$ complexes is much smaller than the electrostatic part of the interaction energy, it is clear from our analysis that CT furnishes the *sine qua non* of the anion–water hydrogen bond.

■ ASSOCIATED CONTENT

Ⓢ Supporting Information

The Supporting Information is available free of charge at https://pubs.acs.org/doi/10.1021/acs.jpca.0c11356.

Results of additional calculations (PDF)

■ AUTHOR INFORMATION

Corresponding Author

John M. Herbert − *Department of Chemistry and Biochemistry, The Ohio State University, Columbus, Ohio 43210, United States;* ⓞ orcid.org/0000-0002-1663-2278; Email: herbert@chemistry.ohio-state.edu

Author

Kevin Carter-Fenk − *Department of Chemistry and Biochemistry, The Ohio State University, Columbus, Ohio 43210, United States;* ⓞ orcid.org/0000-0001-8302-4750

Complete contact information is available at:
https://pubs.acs.org/10.1021/acs.jpca.0c11356

Notes

The authors declare the following competing financial interest(s): J.M.H. serves on the board of directors of Q-Chem, Inc.

■ ACKNOWLEDGMENTS

■ REFERENCES

(1) Ayotte, P.; Weddle, G. H.; Kim, J.; Johnson, M. A. Vibrational spectroscopy of the ionic hydrogen bond: Fermi resonances and ion–molecule stretching frequencies in the binary $X^-·H_2O$ (X = Cl, Br, I) complexes via argon predissociation spectroscopy. *J. Am. Chem. Soc.* **1998**, *120*, 12361−12362.

(2) Robertson, W. H.; Johnson, M. A. Molecular aspects of halide ion hydration: The cluster approach. *Annu. Rev. Phys. Chem.* **2003**, *54*, 173−213.

(3) Roscioli, J. R.; Diken, E. G.; Johnson, M. A.; Horvath, S.; McCoy, A. B. Prying apart a water molecule with anionic H-bonding: A comparative spectroscopic study of the $X^-·H_2O$ (X = OH, O, F, Cl, and Br) binary complexes in the 600−3800 cm^{-1} region. *J. Phys. Chem. A* **2006**, *110*, 4943−4952.

(4) Yates, B. F.; Schaefer, H. F., III; Lee, T. J.; Rice, J. E. The infrared spectrum of $F^-·H_2O$. *J. Am. Chem. Soc.* **1988**, *110*, 6327−6332.

(5) Zhao, X. G.; Gonzalez-Lafont, A.; Truhlar, D. G.; Steckler, R. Molecular modeling of solvation. $Cl^-(D_2O)$. *J. Chem. Phys.* **1991**, *94*, 5544−5558.

(6) Combariza, J. E.; Kestner, N. R.; Jortner, J. Surface and interior states of iodide–water clusters. *Chem. Phys. Lett.* **1994**, *221*, 156−160.

(7) Combariza, J. E.; Kestner, N. R.; Jortner, J. Energy-structure relationships for microscopic solvation of anions in water clusters. *J. Chem. Phys.* **1994**, *100*, 2851−2864.

(8) Xantheas, S. S. Quantitative description of hydrogen bonding in chloride–water clusters. *J. Phys. Chem.* **1996**, *100*, 9703−9713.

(9) Baik, J.; Kim, J.; Majumdar, D.; Kim, K. S. Structures, energetics, and spectra of fluoride–water clusters $F^-(H_2O)_n$, n = 1−6: Ab initio study. *J. Chem. Phys.* **1999**, *110*, 9116−9127.

(10) Kim, J.; Lee, H. M.; Suh, S. B.; Majumdar, D.; Kim, K. S. Comparative *ab initio* study of the structures, energetics and spectra of $X^-·(H_2O)_{n=1−4}$ [X = F, Cl, Br, I] clusters. *J. Chem. Phys.* **2000**, *113*, 5259−5272.

(11) Masamura, M. Structres, energetics, and spectra of $Br^-(H_2O)_n$ clusters, n = 1−6: Ab initio study. *J. Chem. Phys.* **2003**, *118*, 6336−6347.

(12) Brown, T. L., Jr.; LeMay, H. E.; Bursten, B. E.; Murphy, C. J. *Chemistry: The Central Science*, 10th ed.; Pearson/Prentice Hall: 2005.

(13) Brown, T. L., Jr.; LeMay, H. E.; Bursten, B. E.; Murphy, C. J.; Woodward, P. M. *Chemistry: The Central Science*, 12th ed.; Pearson: 2012.

(14) Arunan, E.; Desiraju, G. R.; Klein, R. A.; Sadlej, J.; Scheiner, S.; Alkorta, I.; Clary, D. C.; Crabtree, R. H.; Dannenberg, J. J.; Hobza, P.; Kjaergaard, H. G.; Legon, A. C.; Mennucci, B.; Nesbitt, D. J. Defining the hydrogen bond: An account (IUPAC technical report). *Pure Appl. Chem.* **2011**, *83*, 1619−1637.

(15) Puranik, P. G.; Kumar, V. The charge transfer theory of the hydrogen bond. I. Theoretical. *Proc. - Indian Acad. Sci., Sect. A* **1963**, *58*, 29−37.

(16) Ratajczak, H.; Orville-Thomas, W. J. Charge transfer theory and vibrational properties of the hydrogen bond. *J. Mol. Struct.* **1973**, *19*, 237−245.

(17) Ratajczak, H. Charge-transfer properties of the hydrogen bond. I. Theory of the enhancement of dipole moment of hydrogen-bonded systems. *J. Phys. Chem.* **1972**, *76*, 3000−3004.

(18) Ratajczak, H. Charge-transfer properties of the hydrogen bond. II. Charge-transfer theory and the relation between the enhancement of dipole moment and the ionization potential of hydrogen-bonded systems. *J. Phys. Chem.* **1972**, *76*, 3991−3992.

(19) Ratajczak, H.; Orville-Thomas, W. J. Charge-transfer properties of hydrogen bonds. III. Charge-transfer theory and the relation between the energy and the enhancement of dipole moment of hydrogen-bonded complexes. *J. Chem. Phys.* **1973**, *58*, 911−919.

(20) Ratajczak, H.; Orville-Thomas, W. J.; Rao, C. N. R. Charge transfer theory of hydrogen bonds: Relations between vibrational spectra and energy of hydrogen bonds. *Chem. Phys.* **1976**, *17*, 197−216.

(21) Rao, C. N. R.; Dwivedi, P. C.; Ratajczak, H.; Orville-Thomas, W. J. Relation between O−H stretching frequency and hydrogen bond energy: Re-examination of the Badger-Bauer rule. *J. Chem. Soc., Faraday Trans. 2* **1975**, *71*, 955−966.

(22) Scheiner, S. *Hydrogen Bonding. A Theoretical Perspective*; Oxford University Press: 1997.

(23) Badger, R. M.; Bauer, S. H. Spectroscopic studies of the hydrogen bond. II. The shift of the O−H vibrational frequency in the formation of the hydrogen bond. *J. Chem. Phys.* **1937**, *5*, 839−851.

(24) Bhatta, R. S.; Iyer, P. P.; Dhinojwala, A.; Tsige, M. A brief review of Badger−Bauer rule and its validation from a first-principles approach. *Mod. Phys. Lett. B* **2014**, *28*, 1430014.

(25) Boyer, M. A.; Marsalek, O.; Heindel, J. P.; Markland, T. E.; McCoy, A. B.; Xantheas, S. S. Beyond Badger's rule: The origins and generality of the structure−spectra relationship of aqueous hydrogen bonds. *J. Phys. Chem. Lett.* **2019**, *10*, 918−924.

(26) Thompson, W. H.; Hynes, J. T. Frequency shifts in the hydrogen-bonded OH stretch in halide−water clusters. The importance of charge transfer. *J. Am. Chem. Soc.* **2000**, *122*, 6278−6286.

(27) Herbert, J. M.; Head-Gordon, M. Charge penetration and the origin of large O−H vibrational red-shifts in hydrated-electron clusters, $(H_2O)_n^-$. *J. Am. Chem. Soc.* **2006**, *128*, 13932−13939.

(28) Ramos-Cordoba, E.; Lambrecht, D. S.; Head-Gordon, M. Charge-transfer and the hydrogen bond: Spectroscopic and structural implications from electronic structure calculations. *Faraday Discuss.* **2011**, *150*, 345−362.

(29) Rheinecker, J.; Bowman, J. M. The calculated infrared spectrum of Cl⁻H₂O using a new full dimensional *ab initio* potential surface and dipole moment surface. *J. Chem. Phys.* **2006**, *125*, 133206.

(30) Horvath, S.; McCoy, A. B.; Roscioli, J. R.; Johnson, M. A. Vibrationally induced proton transfer in F⁻(H₂O) and F⁻(D₂O). *J. Phys. Chem. A* **2008**, *112*, 12337−12344.

(31) Horvath, S.; McCoy, A. B.; Elliott, B. M.; Weddle, G. H.; Roscioli, J. R.; Johnson, M. A. Anharmonicities and isotopic effects in the vibrational spectra of X⁻·H₂O, ·HDO, and ·D₂O [X = Cl], Br, and I binary complexes. *J. Phys. Chem. A* **2010**, *114*, 1556−1568.

(32) Toffoli, D.; Sparta, M.; Christiansen, O. Vibrational spectroscopy of hydrogen-bonded systems: Six-dimensional simulation of the IR spectrum of F⁻(H₂O) complex. *Chem. Phys. Lett.* **2011**, *510*, 36−41.

(33) Kamarchik, E.; Toffoli, D.; Christiansen, O.; Bowman, J. M. Ab initio potential energy and dipole moment surfaces of the F⁻(H₂O) complex. *Spectrochim. Acta, Part A* **2014**, *119*, 59−62.

(34) Wang, X.-G.; Carrington, T., Jr. Rovibrational levels and wavefunctions of Cl⁻H₂O. *J. Chem. Phys.* **2014**, *140*, 204306.

(35) Sarka, J.; Lauvergnat, D.; Brites, V.; Császár, A. G.; Léonard, C. Rovibrational energy levels of the F⁻(H₂O) and F⁻(D₂O) complexes. *Phys. Chem. Chem. Phys.* **2016**, *18*, 17678−17690.

(36) Bajaj, P.; Wang, X.-G.; Carrington, T., Jr.; Paesani, F. Vibrational spectra of halide-water dimers: Insights on ion hydration from full-dimensional quantum calculations on many-body potential energy surfaces. *J. Chem. Phys.* **2018**, *148*, 102321.

(37) Talbot, J. J.; Yang, N.; Huang, M.; Duong, C. H.; McCoy, A. B.; Steele, R. P.; Johnson, M. A. Spectroscopic signatures of mode-dependent tunnel splitting in the iodide−water binary complex. *J. Phys. Chem. A* **2020**, *124*, 2991−3001.

(38) Robertson, W. H.; Johnson, M. A.; Myshakin, E. M.; Jordan, K. D. Isolating the charge-transfer component of the anionic H bond via spin suppression of the intracluster proton transfer reaction in the NO⁻·H₂O entrance channel complex. *J. Phys. Chem. A* **2002**, *106*, 10010−10014.

(39) Hohenstein, E. G.; Sherrill, C. D. Wavefunction methods for noncovalent interactions. *WIREs Comput. Mol. Sci.* **2012**, *2*, 304−326.

(40) Misquitta, A. J. Intermolecular interactions. In *Handbook of Computational Chemistry*; Leszczynski, J., Ed.; Springer Science + Business Media: 2012; Chapter 6, pp 157−193.

(41) Lao, K. U.; Herbert, J. M. Accurate and efficient quantum chemistry calculations of noncovalent interactions in many-body systems: The XSAPT family of methods. *J. Phys. Chem. A* **2015**, *119*, 235−253.

(42) Patkowski, K. Recent developments in symmetry-adapted perturbation theory. *Wiley Interdiscip. Rev.: Comput. Mol. Sci.* **2020**, *10*, e1452.

(43) Lao, K. U.; Herbert, J. M. Energy decomposition analysis with a stable charge-transfer term for interpreting intermolecular interactions. *J. Chem. Theory Comput.* **2016**, *12*, 2569−2582.

(44) Řezáč, J.; de la Lande, A. Robust, basis-set independent method for the evaluation of charge-transfer energy in noncovalent complexes. *J. Chem. Theory Comput.* **2015**, *11*, 528−537.

(45) Řezác, J.; de la Lande, A. On the role of charge transfer in halogen bonding. *Phys. Chem. Chem. Phys.* **2017**, *19*, 791−803.

(46) Wu, Q.; Ayers, P. W.; Zhang, Y. Density-based energy decomposition analysis for intermolecular interactions with variationally determined intermediate state energies. *J. Chem. Phys.* **2009**, *131*, 164112.

(47) Misquitta, A. J. Charge transfer from regularized symmetry-adapted perturbation theory. *J. Chem. Theory Comput.* **2013**, *9*, 5313−5326.

(48) Kaduk, B.; Kowalczyk, T.; Van Voorhis, T. Constrained density functional theory. *Chem. Rev.* **2012**, *112*, 321−370.

(49) Shao, Y.; et al. Advances in molecular quantum chemistry contained in the Q-Chem 4 program package. *Mol. Phys.* **2015**, *113*, 184−215.

(50) Parker, T. M.; Burns, L. A.; Parrish, R. M.; Ryno, A. G.; Sherrill, C. D. Levels of symmetry adapted perturbation theory (SAPT). I. Efficiency and performance for interaction energies. *J. Chem. Phys.* **2014**, *140*, 094106.

(51) Sinnokrot, M. O.; Sherrill, C. D. Highly accurate coupled cluster potential energy curves for the benzene dimer: Sandwich, T-shaped, and parallel-displaced configurations. *J. Phys. Chem. A* **2004**, *108*, 10200−10207.

(52) Herbert, J. M.; Jacobson, L. D.; Un Lao, K.; Rohrdanz, M. A. Rapid computation of intermolecular interactions in molecular and ionic clusters: Self-consistent polarization plus symmetry-adapted perturbation theory. *Phys. Chem. Chem. Phys.* **2012**, *14*, 7679−7699.

(53) Papajak, E.; Zheng, J.; Xu, X.; Leverentz, H. R.; Truhlar, D. G. Perspectives on basis sets beautiful: Seasonal plantings of diffuse basis functions. *J. Chem. Theory Comput.* **2011**, *7*, 3027−3034.

(54) Lao, K. U.; Schäffer, R.; Jansen, G.; Herbert, J. M. Accurate description of intermolecular interactions involving ions using symmetry-adapted perturbation theory. *J. Chem. Theory Comput.* **2015**, *11*, 2473−2486.

(55) Lao, K. U.; Herbert, J. M. Accurate intermolecular interactions at dramatically reduced cost: XPol+SAPT with empirical dispersion. *J. Phys. Chem. Lett.* **2012**, *3*, 3241−3248.

(56) Jacobson, L. D.; Richard, R. M.; Lao, K. U.; Herbert, J. M. Efficient monomer-based quantum chemistry methods for molecular and ionic clusters. *Annu. Rep. Comput. Chem.* **2013**, *9*, 25−56.

(57) Lao, K. U.; Herbert, J. M. An improved treatment of empirical dispersion and a many-body energy decomposition scheme for the explicit polarization plus symmetry-adapted perturbation theory (XSAPT) method. *J. Chem. Phys.* **2013**, *139*, 034107. Lao, K. U.; Herbert, J. M. Erratum: "An improved treatment of empirical dispersion and a many-body energy decomposition scheme for the explicit polarization plus symmetry-adapted perturbation theory (XSAPT) method" [J. Chem. Phys. 139, 034107 (2013)]. *J. Chem. Phys.* **2014**, *140*, 119901.

(58) Lao, K. U.; Herbert, J. M. Symmetry-adapted perturbation theory with Kohn-Sham orbitals using non-empirically tuned, long-range-corrected density functionals. *J. Chem. Phys.* **2014**, *140*, 044108.

(59) Lao, K. U.; Herbert, J. M. Atomic orbital implementation of extended symmetry-adapted perturbation theory (XSAPT) and benchmark calculations for large supramolecular complexes. *J. Chem. Theory Comput.* **2018**, *14*, 2955−2978.

(60) Carter-Fenk, K.; Lao, K. U.; Liu, K.-Y.; Herbert, J. M. Accurate and efficient *ab initio* calculations for supramolecular complexes:

Symmetry-adapted perturbation theory with many-body dispersion. *J. Phys. Chem. Lett.* **2019**, *10*, 2706−2714.

(61) Liu, K.-Y.; Carter-Fenk, K.; Herbert, J. M. Self-consistent charge embedding at very low cost, with application to symmetry-adapted perturbation theory. *J. Chem. Phys.* **2019**, *151*, 031102.

(62) Bickelhaupt, F. M.; Baerends, E. J. Kohn-Sham density functional theory: Predicting and understanding chemistry. *Reviews in Computational Chemistry* **2007**, *15*, 1.

(63) Becke, A. D. A multicenter numerical integration scheme for polyatomic molecules. *J. Chem. Phys.* **1988**, *88*, 2547−2553.

(64) Medvedev, N. N. The algorithm for three-dimensional Voronoi polyhedra. *J. Comput. Phys.* **1986**, *67*, 223−229.

(65) Aprà, E.; et al. NWChem: Past, present, and future. *J. Chem. Phys.* **2020**, *152*, 184102.

(66) Wu, Q.; Cheng, C.-L.; Van Voorhis, T. Configuration interaction based on constrained density functional theory: A multireference method. *J. Chem. Phys.* **2007**, *127*, 164119.

(67) Hirshfeld, F. L. Bonded-atom fragments for describing molecular charge densities. *Theor. Chem. Acc.* **1977**, *44*, 129−138.

(68) Nalewajski, R. F.; Parr, R. G. Information theory, atoms in molecules, and molecular similarity. *Proc. Natl. Acad. Sci. U. S. A.* **2000**, *97*, 8879−8882.

(69) Parr, R. G.; Ayers, P. W.; Nalewajski, R. F. What is an atom in a molecule? *J. Phys. Chem. A* **2005**, *109*, 3957−3959.

(70) Heidar-Zadeh, F.; Ayers, P. W.; Verstraelen, T.; Vinogradov, I.; Vöhringer-Martinez, E.; Bultinck, P. Information-theoretic approaches to atoms-in-molecules: Hirshfeld family of partitioning schemes. *J. Phys. Chem. A* **2018**, *122*, 4219−4245.

(71) Holmberg, N.; Laasonen, K. Efficient constrained density functional theory implementation for simulation of condensed phase electron transfer reactions. *J. Chem. Theory Comput.* **2017**, *13*, 587−601.

(72) Bultinck, P.; Van Alsenoy, C.; Ayers, P. W.; Carbó-Dorca, R. Critical analysis and extension of the Hirshfeld atoms in molecules. *J. Chem. Phys.* **2007**, *126*, 144111.

(73) Verstraelen, T.; Ayers, P. W.; Van Speybroeck, V.; Waroquier, M. Hirshfeld-E partitioning: AIM charges with an improved trade-off between robustness and accurate electrostatics. *J. Chem. Theory Comput.* **2013**, *9*, 2221−2225.

(74) Lillestolen, T. C.; Wheatley, R. J. Redefining the atom: Atomic charge densities produced by an iterative stockholder approach. *Chem. Commun.* **2008**, 5909−5911.

(75) Bultinck, P.; Cooper, D. L.; Van Neck, D. Comparison of the Hirshfeld-I and iterated stockholder atoms in molecules schemes. *Phys. Chem. Chem. Phys.* **2009**, *11*, 3424−3429.

(76) Dasgupta, S.; Herbert, J. M. Standard grids for high-precision integration of modern density functionals: SG-2 and SG-3. *J. Comput. Chem.* **2017**, *38*, 869−882.

(77) Arismendi-Arrieta, D. J.; Riera, M.; Bajaj, P.; Prosmiti, R.; Paesani, F. i-TTM model for ab initio-based ion−water interaction potentials. 1. Halide−water potential energy functions. *J. Phys. Chem. B* **2016**, *120*, 1822−1832.

(78) Adler, T. B.; Knizia, G.; Werner, H.-J. A simple and efficient CCSD(T)-F12 approximation. *J. Chem. Phys.* **2007**, *127*, 221106.

(79) Feller, D.; Peterson, K. A. An expanded calibration study of the explicitly correlated CCSD(T)-F12b method using large basis set standard CCSD(T) atomization energies. *J. Chem. Phys.* **2013**, *139*, 084110.

(80) Feller, D. Statistical electronic structure calibration study of the CCSD(T*)-F12b method for atomization energies. *J. Phys. Chem. A* **2015**, *119*, 7375−7387.

(81) Kesharwani, M. K.; Sylvetsky, N.; Köhn, A.; Tew, D. P.; Martin, J. M. L. Do CCSD and approximate CCSD-F12 variants converge to the same basis set limits? The case of atomization energies. *J. Chem. Phys.* **2018**, *149*, 154109.

(82) Schlicht, F.; Entfellner, M.; Boesl, U. Anion ZEKE-spectroscopy of the weakly bound iodine water complex. *J. Phys. Chem. A* **2010**, *114*, 11125−11132.

(83) Chamorro, Y.; Flórez, E.; Maldonado, A.; Aucar, G.; Restrepo, A. Microsolvation of heavy halides. *Int. J. Quantum Chem.* **2020**, e26571.

(84) Lee, H. M.; Kim, K. S. Structures and spectra of iodide−water clusters $I^-(H_2O)_{n=1-6}$: An *ab initio* study. *J. Chem. Phys.* **2001**, *114*, 4461−4471.

(85) Sherrill, C. D. Energy component analysis of π interactions. *Acc. Chem. Res.* **2013**, *46*, 1020−1028.

(86) Ryno, S. M.; Risko, C.; Brédas, J.-L. Noncovalent interactions and impact of charge penetration effects in linear oligoacene dimers and single crystals. *Chem. Mater.* **2016**, *28*, 3990−4000.

(87) Carter-Fenk, K.; Herbert, J. M. Electrostatics does not dictate the slip-stacked arrangement of aromatic π−π interactions. *Chem. Sci.* **2020**, *11*, 6758−6765.

(88) Carter-Fenk, K.; Herbert, J. M. Reinterpreting π-stacking. *Phys. Chem. Chem. Phys.* **2020**, *22*, 24870−24886.

(89) Gryn'ova, G.; Corminboeuf, C. Steric "attraction": Not by dispersion alone. *Beilstein J. Org. Chem.* **2018**, *14*, 1482−1490.

(90) Thole, B. T. Molecular polarizabilities calculated with a modified dipole interaction. *Chem. Phys.* **1981**, *59*, 341−350.

(91) Ren, P.; Wu, C.; Ponder, J. W. Polarizable atomic multipole-based molecular mechanics for organic molecules. *J. Chem. Theory Comput.* **2011**, *7*, 3143−3161.

(92) Shi, Y.; Xia, Z.; Zhang, J.; Best, R.; Wu, C.; Ponder, J. W.; Ren, P. Polarizable atomic multipole-based AMOEBA force field for proteins. *J. Chem. Theory Comput.* **2013**, *9*, 4046−4063.

(93) Rackers, J. A.; Wang, Q.; Liu, C.; Piquemal, J.-P.; Ren, P.; Ponder, J. W. An optimized charge penetration model for use with the AMOEBA force field. *Phys. Chem. Chem. Phys.* **2017**, *19*, 276−291.

(94) Ren, P.; Ponder, J. W. Polarizable atomic multipole water model for molecular mechanics simulation. *J. Phys. Chem. B* **2003**, *107*, 5933−5947.

(95) Burnham, C. J.; Xantheas, S. S. Development of transferable interaction models for water. IV. A flexible, all-atom polarizable potential (TTM2-F) based on geometry dependent charges derived from an *ab initio* monomer dipole moment surface. *J. Chem. Phys.* **2002**, *116*, 5115−5124.

(96) Fanourgakis, G. S.; Xantheas, S. S. The flexible, polarizable, Thole-type interaction potential for water (TTM2-F) revisited. *J. Phys. Chem. A* **2006**, *110*, 4100−4106.

(97) Fanourgakis, G. S.; Xantheas, S. S. Development of transferable interaction potentials for water. V. Extension of the flexible, polarizable, Thole-type model potential (TTM3-F, v. 3.0) to describe the vibrational spectra of water clusters and liquid water. *J. Chem. Phys.* **2008**, *128*, 074506.

(98) Babin, V.; Leforestier, C.; Paesani, F. Development of a "first principles" water potential with flexible monomers: Dimer potential energy surface, VRT spectrum, and second virial coefficient. *J. Chem. Theory Comput.* **2013**, *9*, 5395−5403. Babin, V.; Leforestier, C.; Paesani, F. Erratum: Development of a "First-Principles" Water Potential with Flexible Monomers: Dimer Potential Energy Surface, VRT Spectrum, and Second Virial Coefficient. *J. Chem. Theory Comput.* **2014**, *10*, 2212.

(99) Grossfield, A.; Ren, P.; Ponder, J. W. Ion solvation thermodynamics from simulation with a polarizable force field. *J. Am. Chem. Soc.* **2003**, *125*, 15671−15682.

(100) Jiao, D.; King, C.; Grossfield, A.; Darden, T. A.; Ren, P. Simulation of Ca^{2+} and Mg^{2+} solvation using polarizable atomic multipole potential. *J. Phys. Chem. B* **2006**, *110*, 18553−18559.

(101) Jacobson, L. D.; Williams, C. F.; Herbert, J. M. The static-exchange electron-water pseudopotential, in conjunction with a polarizable water model: A new Hamiltonian for hydrated-electron simulations. *J. Chem. Phys.* **2009**, *130*, 124115.

(102) Jacobson, L. D.; Herbert, J. M. A one-electron model for the aqueous electron that includes many-body electron-water polarization: Bulk equilibrium structure, vertical electron binding energy, and optical absorption spectrum. *J. Chem. Phys.* **2010**, *133*, 154506.

(103) Riera, M.; Götz, A. W.; Paesani, F. The i-TTM model for *ab initio*-based ion−water interaction potentials. II. Alkali metal ion−

water potential energy functions. *Phys. Chem. Chem. Phys.* **2016**, *18*, 30334−30342.

(104) Paesani, F.; Bajaj, P.; Riera, M. Chemical accuracy in modeling halide ion hydration from many-body representations. *Adv. Phys. X* **2019**, *4*, 1631212.

(105) Stone, A. J. Are halogen bonded structures electrostatically driven? *J. Am. Chem. Soc.* **2013**, *135*, 7005−7009.

(106) Shahi, A.; Arunan, E. Why are hydrogen bonds directional? *J. Chem. Sci.* **2016**, *128*, 1571−1577.

(107) Arunan, E.; Desiraju, G. R.; Klein, R. A.; Sadlej, J.; Scheiner, S.; Alkorta, I.; Clary, D. C.; Crabtree, R. H.; Dannenberg, J. J.; Hobza, P.; Kjaergaard, H. G.; Legon, A. C.; Mennucci, B.; Nesbitt, D. J. Definition of they hydrogen bond (IUPAC recommendations 2011). *Pure Appl. Chem.* **2011**, *83*, 1637−1641.

(108) Ranganathan, A.; Kulkarni, G. U.; Rao, C. N. R. Understanding the hydrogen bond in terms of the location of the bond critical point and the geometry of the lone pairs. *J. Phys. Chem. A* **2003**, *107*, 6073−6081.

(109) Ronca, E.; Belpassi, L.; Tarantelli, F. A quantitative view of charge transfer in the hydrogen bond: The water dimer case. *ChemPhysChem* **2014**, *15*, 2682−2687.

(110) Espinosa, E.; Alkorta, I.; Elguero, J.; Molins, E. From weak to strong interactions: A comprehensive analysis of the topological and energetic properties of the electron density distribution involving X−H··· F−Y systems. *J. Chem. Phys.* **2002**, *117*, 5529−5542.

(111) Mata, I.; Molins, E.; Alkorta, I.; Espinosa, E. Tuning the interaction energy of hydrogen bonds: The effect of the substituent. *J. Phys. Chem. A* **2011**, *115*, 12561−12571.

(112) Umeyama, H.; Morokuma, K. The origin of hydrogen bonding. An energy decomposition study. *J. Am. Chem. Soc.* **1977**, *99*, 1316−1332.

(113) Reed, A. E.; Weinhold, F. Natural bond orbital analysis of near-Hartree−Fock water dimer. *J. Chem. Phys.* **1983**, *78*, 4066−4073.

(114) Stone, A. J. Natural bond orbitals and the nature of the hydrogen bond. *J. Phys. Chem. A* **2017**, *121*, 1531−1534.

(115) Weinhold, F.; Glendening, E. D. Comment on "Natural bond orbitals and the nature of the hydrogen bond. *J. Phys. Chem. A* **2018**, *122*, 724−732.

(116) Stone, A. J.; Szalewicz, K. Reply to "Comment on 'Natural bond orbitals and the nature of the hydrogen bond'". *J. Phys. Chem. A* **2018**, *122*, 733−736.

(117) Stone, A. J.; Misquitta, A. J. Charge-transfer in symmetry-adapted perturbation theory. *Chem. Phys. Lett.* **2009**, *473*, 201−205.

(118) Ohio Supercomputer Center; http://osc.edu/ark:/19495/f5s1ph73.